1 **Seasonal variations in composition and sources of atmospheric ultrafine particles**
2 **in urban Beijing based on near-continuous measurements**

3 *Xiaoxiao Li[1,2], Yijing Chen[1], Yuyang Li[1], Runlong Cai[3], Yiran Li[1], Chenjuan Deng[1], Chao Yan[3,4],*

4 *Hairong Cheng[2], Yongchun Liu[4], Markku Kulmala[3,4], Jiming Hao[1], James N. Smith[5*], and Jingkun*

5 *Jiang[1*]*

6 [1] State Key Joint Laboratory of Environment Simulation and Pollution Control, School of Environment,
7 Tsinghua University, 100084 Beijing, China

8 [2] School of Resources and Environmental Sciences, Wuhan University, 430072 Wuhan, China

9 [3] Institute for Atmospheric and Earth System Research / Physics, Faculty of Science, University of
10 Helsinki, 00014 Helsinki, Finland

11 [4] Aerosol and Haze Laboratory, Beijing Advanced Innovation Center for Soft Matter Science and
12 Engineering, Beijing University of Chemical Technology, 100029 Beijing, China

13 [5] Chemistry Department, University of California, Irvine, CA 92697, USA

14 *Correspondence to:* Jingkun Jiang (jiangjk@tsinghua.edu.cn) and James N. Smith
15 (jimsmith@uci.edu)

16

17 **Abstract.** Understanding the composition and sources of atmospheric ultrafine particles (UFPs) is
18 essential in evaluating their exposure risks. It requires long-term measurements with high time
19 resolution, which are to date scarce. We performed near-continuous measurements of UFP composition
20 during four seasons in urban Beijing using a thermal desorption chemical ionization mass spectrometer,
21 accompanied by real-time size distribution measurements. We found that UFPs in urban Beijing are
22 dominated by organic components, varying seasonally from 68 to 81%. CHO organics are the most
23 abundant in summer, while sulfur-containing organics, some nitrogen-containing organics, nitrate, and
24 chloride are the most abundant in winter. With the increase of particle diameter, the contribution of
25 CHO organics decreases, while that of sulfur-containing and nitrogen-containing organics, nitrate, and
26 chloride increase. Source apportionment analysis of the UFP organics indicates contributions from
27 cooking and vehicle sources, photooxidation sources enriched in CHO organics, and
28 aqueous/heterogeneous sources enriched in nitrogen- and sulfur-containing organics. The increased
29 contributions of cooking, vehicle, and photooxidation components are usually accompanied by
30 simultaneous increases in UFP number concentrations related to cooking emission, vehicle emission,
31 and new particle formation, respectively. While the increased contribution of the
32 aqueous/heterogeneous composition is usually accompanied by the growth of UFP mode diameters.
33 The highest UFP number concentrations in winter are due to the strongest new particle formation, the
34 strongest local primary particle number emissions, and the slowest condensational growth of UFPs to
35 larger sizes. This study provides a comprehensive understanding of urban UFP composition and
36 sources and offers valuable datasets for the evaluation of UFP exposure risks.

1. Introduction

Ultrafine particles (UFPs, particles with diameters smaller than or equal to 100 nm) have significant effects on human health (HEI, 2013; Ohlwein et al., 2019; WHO, 2013) and global climate (Kulmala et al., 2004; Pierce and Adams, 2007). Their human exposure risks and climate effects are highly related to their composition and size (Oberdorster et al., 2005; Pierce and Adams, 2007). To better evaluate the exposure risks of UFPs and to formulate corresponding air quality guidelines, the World Health Organization made several recommendations to guide measurements and regulations of UFPs in 2021 (Organization, 2021). They emphasized that local understanding of UFP origins and their chemical composition are scarce in most parts of the world.

Current field studies of atmospheric UFP composition and their source apportionment are mostly based on offline sampling. These measurements usually use a size-resolving impactor to collect UFPs on filters for tens of hours to several days (Cabada et al., 2004; Cass et al., 2000; Ham and Kleeman, 2011; Herner et al., 2005; Kleeman et al., 2009; Massling et al., 2009; Xue et al., 2019; Xue et al., 2020a; Xue et al., 2020b; Zhao et al., 2017). They found that organic carbon, sulfate, and nitrate could account for 50-90% of the detected compounds, and the composition could vary greatly with UFP sizes due to different sources and atmospheric evolutions (Cabada et al., 2004; Herner et al., 2005; Massling et al., 2009). For source apportionment, the Chemical Mass Balance analysis was often used which relies heavily on the source profiles and the limited numbers of molecular markers (Ham and Kleeman, 2011; Kleeman et al., 2009; Xue et al., 2019). The identified sources include meat cooking, gasoline, diesel, motor oil, and wood burning. However, these offline explorations can not capture the high temporal variability in size-resolved UFP composition and sources, nor can they distinguish primary UFPs from secondary sources, e.g., new particle formation, due to the lack of tracers and composition profiles for secondary sources. Simultaneous real-time measurements of UFP composition and size distributions are needed to accurately identify both primary and secondary sources.

Using a thermal desorption chemical ionization mass spectrometer (TDCIMS), the size-resolved composition of UFPs can be measured with a resolution of tens of minutes (Li et al., 2021; Smith et al., 2004). Previously, it has been used in a number of sites for short-term measurements and found distinct characteristics for UFPs in urban (Li et al., 2022a; Li et al., 2021; Smith et al., 2008; Smith et al., 2005), rural (Lawler et al., 2020; Smith et al., 2010), and remote areas (Glicker et al., 2019; Lawler et al., 2018; Lawler et al., 2021; Lawler et al., 2014). For instance, UFPs in urban areas have more nitrogen- and sulfur-containing organics (Smith et al., 2005; Winkler et al., 2012), while those at forest sites have more CHO organics (Glicker et al., 2019; Lawler et al., 2018). With these near-continuous measurements, unique sources such as fungal bursts (Lawler et al., 2020) and sea-salt nanoparticles (Lawler et al., 2014) were identified and the mechanisms of new particle formation were examined (Li et al., 2022a). Source apportionment analysis was performed for the high time-resolution TDCIMS results in Amazon Basin to isolate anthropogenic UFPs from background UFPs (Glicker et al., 2019).

73   These analyses mainly focused on short-term analysis covering several weeks. To address the UFP
74   composition and sources from a more comprehensive view, there is an urgent need for long-term and
75   high-time-resolution measurements in diverse environments.

76   The primary and secondary sources of particles in urban atmospheres usually show significant seasonal
77   characteristics. Thus, addressing the seasonal variations of UFPs, as well as their governing factors, is
78   fundamental to evaluating their long-term impacts. For fine particles in Beijing, coal combustion is
79   more abundant in winter due to domestic heating in the surrounding regions (Sun et al., 2015; Zhang
80   et al., 2013), biomass burning is more abundant in harvest seasons (Zhang et al., 2008), and dust storms
81   are more frequent in spring (Xu et al., 2020; Zhang et al., 2013). Besides these primary sources,
82   previous studies on larger particles showed higher oxidation states of organic aerosols in summer due
83   to stronger photochemical processes (Hu et al., 2017; Ma et al., 2022; Sun et al., 2018). However,
84   considering the short lifetime of UFPs, seasonal variations of the composition and sources of UFPs are
85   likely different. For example, as an important source of UFPs, new particle formations in Beijing were
86   observed to be the weakest in summer and strongest in winter due to temperature variations (Deng et
87   al., 2020; Li et al., 2020; Wu et al., 2007). Similar to Beijing, seasonal variations of UFP composition
88   based on high time-resolution measurements are also scarce for other atmospheric sites.

89   Here, we performed near-continuous measurements of UFP composition and size distributions over
90   four seasons in a typical megacity of Beijing with ~22 million people. The UFP composition, its size
91   dependence, and seasonal variability were analyzed. Several molecular markers from cooking and
92   vehicle emissions were identified. These markers were combined with the Positive Matrix
93   Factorization (PMF) analysis to address contributions from primary and secondary sources of UFPs.
94   The aerosol General Dynamic Equation (GDE) was used to quantify the emission rates of primary
95   UFPs and the formation rates of secondary UFPs. The driving factors for the seasonal variations of
96   UFP composition and number concentrations were identified.

97   **2. Methods**

98   **2.1 Field measurements.**

99   The sampling site is on the fifth floor of a building on the west campus of Beijing University of
100   Chemical Technology (39°94′N, 116°30′E) (Liu et al., 2020). The site is a typical urban site,
101   surrounded by residential and commercial buildings. Three trafficked roads are 130~565 m away from
102   the sites. UFP composition, particle number-size distribution, trace gases, and meteorological
103   conditions were measured over four seasons between Dec. 2019 and Aug. 2021. An overall of 149
104   days' TDCIMS measurements were used for analysis, with at least three weeks' data for each season.
105   Details of the sampling periods are described in Table S1.

106   UFP composition was measured by the TDCIMS using the "bulk collection mode" (Li et al., 2021;
107   Smith et al., 2004). The TDCIMS collects pre-charged particles on a high voltage-biased Pt filament

108 and then vaporizes the particles for analysis by a chemical ionization high-resolution time-of-flight
109 mass spectrometer (CI-HTOF, Aerodyne Research Inc. and Tofwerk AG). The particle electrostatic
110 collection efficiency on the filament decreases rapidly with increasing particle size, ensuring that the
111 collected particle mass is mainly from UFPs (Li et al., 2021). Using O_2^- as the reagent ion, sulfate,
112 nitrate, chloride, and most of the oxygenated organics can be measured, while black carbon,
113 hydrocarbon compounds, and bases such as ammonium and aminium cannot be detected. Every
114 sampling cycle is followed by a background cycle where no voltages are applied to the Pt filament for
115 particle collection. The signals from the background cycle are subtracted from the sampling cycle to
116 exclude minor influences from the gas phase compounds. Each analysis cycle (including a sample and
117 a background cycle) is set to be 10-40 min, depending on the estimated sample mass. The detailed
118 principles, operations, and quantifications of the TDCIMS are the same as the "bulk collection mode"
119 described in our previous study (Li et al., 2021).

120 The particle number size distributions from 1 nm to 10 μm were measured using a home-built particle
121 size distribution system (PSD, 3 nm–10 μm) and a diethylene glycol scanning mobility particle
122 spectrometer (DEG-SMPS, 1–7.5 nm). The configuration and operation of the PSD are the same as
123 described in our previous studies (Cai et al., 2017). The time resolution of the measurement is 5 min.
124 The number and mass concentrations of atmospheric UFPs were estimated via the integration of size
125 distribution measurements, assuming spherical particles with a density of 1.4 g cm^{-3}.

126 Other parameters used in this study include the meteorological conditions measured by the
127 meteorology stations (AWS310, Vaisala Inc., Finland) and trace gases measured by the trace gas
128 analyzers (TGA, Thermo Fisher). The mixing layer height (MLH) was estimated from the vertical
129 profiles measured by a ceilometer (CL51, Vaisala Inc., Finland) and a three-step idealized-profile
130 method was used to estimate the MLH (Eresmaa et al., 2012).

2.2 Source apportionment of UFP composition.

131
132 The Igor-based interface SoFi (solution finder, version 6.5) and ME-2 (Canonaco et al., 2013) were
133 used for the PMF analysis to analyze the sources of organics in UFPs. The integrated thermal
134 desorption signals of organic peaks with m/z between 100 and 300 measured by the TDCIMS were
135 used as the input data matrix. The integrated thermal desorption signals from the background samples
136 were used to derive the input error matrix. The best solution in each season was chosen according to
137 Q/Q$_{exp}$, the similarities between m/z profiles, time series, and diurnal variations of the factors. The
138 correlations between each factor and the measured key species, trace gas, and PM$_{2.5}$ were calculated
139 for better identification of the factors. It should be noted that there were also many peaks with m/z
140 below 100, but a large fraction of them was from thermal decomposition, and their inclusion would
141 add great complexity to the factor assignments. The signal intensity instead of the mass concentration
142 was used because sensitivity quantification of the TDCIMS was based on the calibration of limited
143 numbers of compounds which may induce unknown uncertainties when quantifying the sources. As a

144   result, the signal intensity measured by the TDCIMS is reported for reference and the relative
145   variations of detected species are studied rather than their estimated ambient concentrations.

146   **2.3 Quantifying source and loss terms of UFP number concentrations.**

147   In the measured size distribution plots, there are usually abrupt increases in UFP number concentration.
148   During new particle formation (NPF) periods, the abrupt increases of UFPs are usually accompanied
149   by a burst of sub-3 nm particles and usually start from noontime. During non-NPF periods, the abrupt
150   increases of UFPs are usually accompanied by an increase in primary emission tracers (as will be
151   shown in Section 3.2). We apply the GDE to quantify the new particle formation rates (J) and primary
152   particle number emission rates (E) at the observation site. The calculation of J follows those described
153   in previous studies (Cai and Jiang, 2017; Cai et al., 2017). The calculation of $E_{[i,j]}$ (m^{-3} s^{-1}), the particle
154   emission rates in the size range of [d_i, d_j], follows Eq. 1 (Cai et al., 2018; Kontkanen et al., 2020)
155   during non-NPF periods.

156                         $$E_{[i,j]} = \frac{dN_{[i,j]}}{dt} + GR(n_j - n_i) + CoagSnk_{[i,j]} - CoagSrc_{[i,j]} - TR_{[i,j]} \qquad \text{(Eq. 1)}$$

157   Where $\frac{dN_{[i,j]}}{dt}$ (m^{-3} s^{-1}) is the variation of the particle number concentration in the size range of [d_i,

158   d_j] during the period of dt (s^{-1}); $GR(n_j - n_i)$ (m^{-3} s^{-1}) is the net condensation growth term, GR (m s^{-1}) is
159   the condensational growth rate of particle d_i, and n_i (m^{-4}) is the particle number size distribution
160   function for particle d_i; $CoagSrc_{[i,j]}$ and $CoagSnk_{[i,j]}$ (m^{-3} s^{-1}) are the coagulation source and sink terms;
161     $TR_{[i,j]}$ is the transport term. Overall, 33 size bins were included in the size range of 3-50 nm.

162   The term $\frac{dN_{[i,j]}}{dt}$ and $CoagSnk_{[i,j]}$ can be directly calculated from the size distribution data (Cai et al.,

163   2018). GR is calculated by the theoretical condensation of the condensable vapors, that is the sum of
164   H_2SO_4 and condensable organic vapor concentrations. Here, we regard condensable organic vapors as
165   oxygenated organic molecules (OOMs) with saturation vapor pressure lower than 0.3 μg m^{-3} as in our
166   previous studies (Li et al., 2022a; Qiao et al., 2021). Since not all the observation days were equipped
167   with the measurements of condensable vapors, we adopted seasonal-dependent GR derived from
168   seasonal average condensable vapor concentrations reported in our previous study, that is 1.2×10^7,
169   9.9×10^7, 1.2×10^8, and 5.0×10^7 cm^{-3} for winter, spring, summer, and autumn (Qiao et al., 2021),
170   respectively. For particles smaller than 50 nm, $CoagSrc_{[i,j]}$ term can be neglected; for particles smaller
171   than 5 nm, the uncertainties will be very large for E. We only calculated E_{3-50} in this study and
172     $CoagSrc_{[i,j]}$ was thus neglected. Generally, $TR_{[i,j]}$ term cannot be quantified using the mathematic
173   method. As our previous study has indicated there was no significant transport term on a long-term
174   time scale (Kontkanen et al., 2020), we initially assumed that $TR_{[i,j]}$ equals 0. Another assumption is
175   that the influences from the variation in MLH are neglected. We briefly explore how the assumptions

176 of $TR_{[i,j]}$ and MLH influence the results in the next paragraph.

177 On the particle size distribution plots, we notice that the abrupt appearance of particles during non-
178 NPF days usually happens in the early morning (6:00-9:00) and late afternoon (17:00-20:00) (Figure
179 S1). The afternoon peak is accompanied by a decrease in MLH and an increase in particle numbers in
180 all sizes within the range of 3-50 nm, thus the abrupt increase in particle number concentration could
181 be due to the combined effects of MLH, transport, and emission. The morning peak is accompanied
182 by the increase in MLH, which should decrease particle number concentrations, and the increase in
183 particle number is only observed for 3-30 nm particles but not for 30-50 nm. Thus, the increasing
184 morning peak could only be caused by the primary emission of 3-30 nm particles. As a result, the 3-
185 30 nm particle emission rate during 6:00-9:00 is calculated to represent the average primary particle
186 emission rates for each day. It should be noted that the emission rates during 6:00-9:00 may be
187 underestimated due to the increase of MLH, and the emission rates only represent the increasing rates
188 of primary particles at the observational site, not the direct emission rates from the sources.

189 ## 3. Results and discussion

190 ### 3.1 UFP concentration, composition, and seasonal variability

191 The overall concentration of UFPs is the highest in winter and the lowest in summer. The UFP number
192 concentrations expressed in mean ± standard deviation are $(1.7\pm1.2)\times10^4$, $(1.5\pm1.1)\times10^4$,
193 $(1.1\pm0.7)\times10^4$, and $(1.5\pm0.9)\times10^4$ cm^{-3} (Figure 1a) and the UFP mass concentrations are 1.3±0.9,
194 1.2±0.9, 1.0±0.6, and 1.2±0.7 µg m^{-3} (Figure 1b) for winter, spring, summer, and autumn, respectively.
195 The seasonal variations are partly caused by the variation in MLH (Figure S2), while the other driving
196 factors are related to the source and loss terms of UFPs and will be further discussed in Section 3.3.
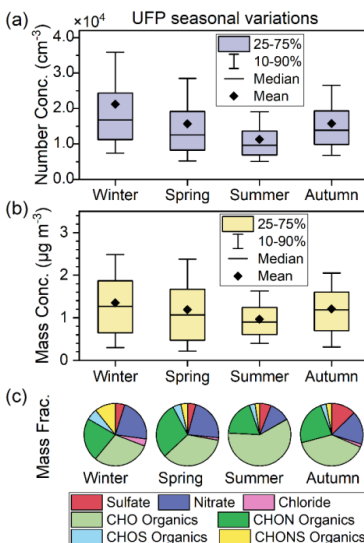
197

198   **Figure 1**. Seasonal variations of UFP concentrations and composition in urban Beijing. (a) UFP
199   number concentrations in the size range of 3-100 nm. (b) UFP mass concentrations integrated from
200   size distribution measurements, assuming spherical particles with a density of 1.4 g cm^{-3}. (c) Mass
201   fractions of the components measured by the TDCIMS in negative ion mode.

202   The detected UFP composition is dominated by organics (68-81% for mass fraction), with minor
203   contributions from nitrate (11-22%), sulfate (4-13%), and chloride (0.1-4%) over all four seasons
204   (Figure 1c). The organic species include CHO, CHON, CHOS, and CHONS organics, contributing 30-
205   59%, 19-29%, 3-6%, and 2-11% mass concentrations of the detected UFP compounds, respectively.
206   The detected particulate species are similar for all four seasons as indicated by the similarities in the
207   mass defect plots (Figure S3). The measured composition is consistent with the offline results from
208   Beijing, which showed that organics were the most abundant in UFPs (Massling et al., 2009; Zhao et
209   al., 2017). It should be noted that the collected mass integrated from the TDCIMS signals is ~50% of
210   the total collected mass estimated from the size distributions (Figure S4). This is possibly due to the
211   uncertainties in the quantification methods or because some UFP compounds (e.g., ammonia, amines,
212   black carbon, and alkanes) cannot be ionized by O_2^- in the TDCIMS. However, as the mass estimated
213   from the two methods are in good correlation, we assume that the TDCIMS-measured composition is
214   representative of UFP composition. As some of the particulate CHON, CHOS, and CHONS organics
215   would decompose to CHO fragments in the TDCIMS during the thermal desorption process, there may
216   be some underestimation of CHON and CHOS/CHONS organics and overestimation of CHO organics.

217   A major seasonal difference in UFP chemical composition is that the highest fractions of slow-
218   desorbed CHO organics are observed in summer (59%), which may be related to the strongest solar
219   radiation and lowest NO_x concentrations. On the one hand, the appearance of most CHO organic ions
220   during temperature ramping of the Pt wire during TDCIMS analysis occurs later, thus at a higher
221   temperature, compared to nitrate and chloride, while slightly earlier, or at a lower desorption
222   temperature, compared to sulfate (Figure S5). The higher temperature desorption, which we refer to as
223   "slowly-desorbed," indicates that these species must be low-volatility compounds or the corresponding
224   thermal decomposition fragments. On the other hand, the overall CHO organic mass has an afternoon
225   peak at ~14:00, and its diurnal variation is consistent with that for O_3 in summer (Figure S6), indicating
226   they might be related to photooxidation chemistry. Based on these, we hypothesize that CHO organics
227   in the UFPs are mostly from the partitioning of low-volatility compounds originating from the gas-
228   phase oxidation. Thus, the higher CHO fractions in summer are due to the strongest solar radiation,
229   which benefits the gaseous photooxidation, and the lowest NO_x (Figure S2), which contributes to the
230   formation of CHO organics over CHON organics (Yan et al., 2020; Ye et al., 2019).

231   Another seasonal difference is that higher fractions of fast-desorbed species are measured in winter,
232   including nitrate, chloride, and some CHON (e.g., $C_6H_4NO_3^-$, nitrophenols) organic compounds. These
233   species are all desorbed at lower temperatures (Figure S5) and their concentrations in UFPs are

234   negatively correlated to ambient temperature (Figure S7), indicating their relatively higher volatility.
235   Thus, the higher fractions in winter are mainly governed by the temperature-dependent partitioning of
236   these compounds. It should be noted that CHONS organic (e.g., deprotonated aminomethanesulfonic
237   acid $CH_4NSO_3^-$ and deprotonated taurine $C_2H_6NSO_3^-$) fractions also increase in winter. Previously,
238    $CH_4NSO_3^-$ and $C_2H_6NSO_3^-$ were reported to be formed in the gas phase through the reaction between
239   SO_3 and amines under dry conditions (Li et al., 2018; Sarkar et al., 2019), which is favored in winter
240   Beijing where the ambient relative humidity is relatively low. The seasonal variations of these CHONS
241   species are different from those in larger particles where S-containing organics are mainly
242   organosulfates from primary emissions or heterogeneous/aqueous reactions (Ma et al., 2022).

243   The composition of UFPs also varies greatly with particle size. As shown in Figure 2, the most
244   significant size-dependent variations were observed for nitrate and CHO organics. The nitrate fraction
245   increases significantly with increasing particle diameter, probably due to the Kelvin effects that prevent
246   it from partitioning to small particles, or due to an increase in aqueous/heterogeneous processes at
247   larger particle sizes. The CHO organic fraction decreases significantly with increased particle size,
248   possibly due to its low volatility that favors smaller particles compared to the high-volatility
249   compounds. Compared to CHO organics, the relative contributions of N- and S-containing organics
250   increase with particle size, possibly due to higher volatility or the aqueous/heterogeneous formation as
251   particles grow. The sulfate fraction does not change significantly with particle sizes, possibly due to
252   the opposite size-dependence of condensational growth of H_2SO_4 and the aqueous/heterogeneous
253   formation of sulfate.
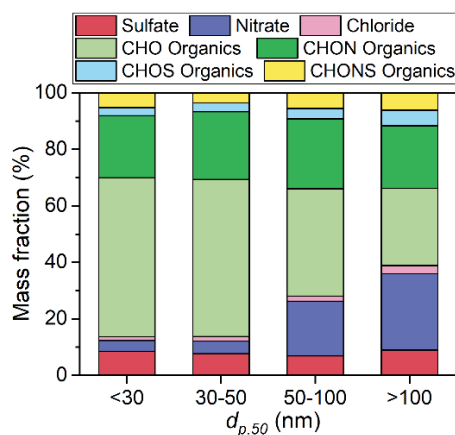
254

255   **Figure 2**. Size-dependent composition of UFPs. UFP composition mass fraction variation with the
256   representing particle size $d_{p,50}$. $d_{p,50}$ corresponds to 50% volume mean diameter of particles collected
257   on the TDCIMS filament.

3.2 Sources of UFP organics and their seasonal variabilities

As organics are the main components of UFPs, PMF source apportionments were performed for the organic compounds. Five factors were identified in each season. The factor profiles and their diurnal variations in winter are shown in Figure 3, and the results in other seasons are shown in Figure S8-10. The correlations between PMF factors and key UFP components, trace gases, meteorology parameters, and PM$_{2.5}$ for the four seasons are shown in Figure S11.
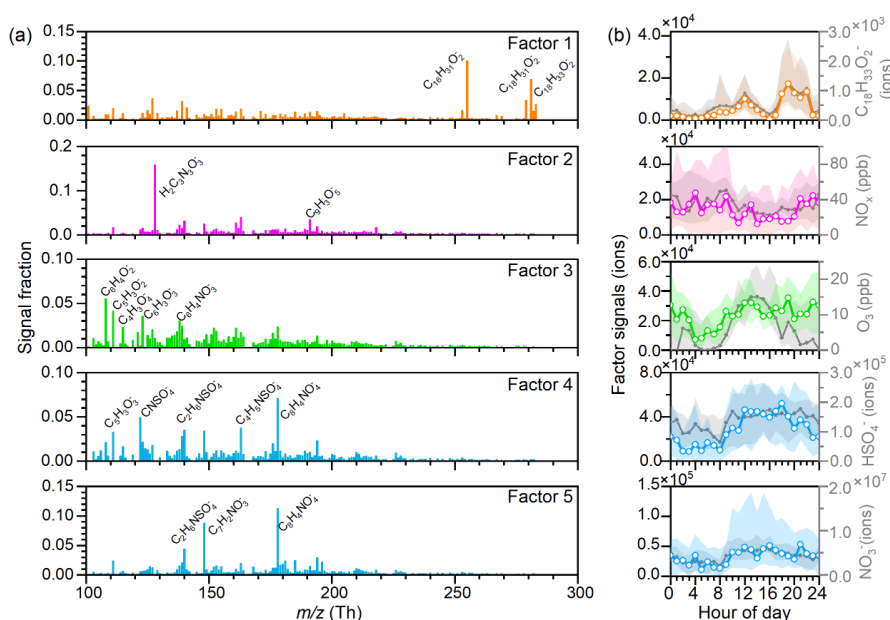
Figure 3. Source apportionment of the UFP organic composition (m/z 100-300) measured by the TDCIMS in winter. (a) m/z profiles of the five PMF factors; (b) diurnal variations of each factor and their related terms.

Factor 1 and factor 2 are identified as cooking-related and vehicle-related sources, respectively. Factor 1 is enriched in C$_{16}$H$_{31}$O$_2^-$, C$_{18}$H$_{31}$O$_2^-$, and C$_{18}$H$_{33}$O$_2^-$ (assigned to deprotonated palmitic acid, linoleic acid, and oleic acids, respectively). Previous studies have revealed that saturated and unsaturated fatty acids are the major constituents in cooking emissions, accounting for 73-85% of the cooking organic matter, among which palmitic acid and oleic acid can be treated as the unique fingerprints of atmospheric cooking particles (Zhao et al., 2007b, a). Factor 1 and the tracers show clear morning, noon, and evening peaks, corresponding to breakfast, lunch, and dinner times. Factor 2 is enriched in C$_3$N$_3$O$_3$H$_2^-$ (assigned to deprotonated cyanuric acid). Cyanuric acid was previously found with the biggest emission in the urea-based selective catalytic reduction (SCR) technology for the reduction of NO$_x$ from the exhaust of diesel-powered vehicles (Yassine et al., 2012). Factor 2 and the tracer show clear morning peaks corresponding to the morning rush hours, consistent with the diurnal variation of

279 NO_x. These two factors are also identified in the other three seasons (Figure S8-10).

280 Besides these two primary sources, trace amounts of a biomass-burning tracer $C_6H_9O_5^-$ (assigned to
281 deprotonated levoglucosan) were also observed. However, its contribution to the total signal is small
282 and could not be separated into individual factors in the PMF analysis. We thus conclude that the
283 contribution of biomass burning to UFPs might be small in urban Beijing. This is understandable since
284 the burning of high-polluting fuels has been phased out in urban Beijing by the People's Government
285 of Beijing Municipality since 2014 (Municipality, 2014). Although large particles in urban Beijing
286 could be influenced by biomass burning and coal combustion through transport from surrounding
287 regions (Li et al., 2022b; Sun et al., 2015; Zhang et al., 2013; Zhang et al., 2008), UFPs could hardly
288 survive after long-distance transport due to their short lifetime.

289 Factors 3-5 are identified as secondary sources related to photooxidation formation or
290 aqueous/heterogeneous formation. In winter (Figure 3), factor 3 is enriched in slowly-desorbed, low-
291 volatility CHO organics and has daytime peaks at ~12:00-18:00, which is consistent with the diurnal
292 variation of O_3. They should come from gas-phase photooxidation followed by gas-particle
293 partitioning. Factor 4 and factor 5 are enriched in N- or S-containing organics. Their time series and
294 diurnal variability are highly correlated with sulfate, nitrate, $PM_{2.5}$, and relative humidity, indicating
295 the aqueous/heterogeneous formation pathway. Similarly, in spring and autumn, factor 3 is identified
296 as a photooxidation factor that is enriched in CHO organics, and factors 4-5 are identified as
297 aqueous/heterogeneous factors that are enriched in N- or S-containing organics (Figure S8-10).
298 Differently, in summer, factor 4 is identified as a photooxidation factor.

299 Clear seasonal variability of the sources was observed, with the contribution of primary emission
300 factors and aqueous/heterogeneous factors higher in winter and autumn, and the contribution of
301 photooxidation factors higher in summer (Figure S11). The sum of cooking and vehicle sources
302 contributed to 10-35% of the total organic signals in the m/z range of 100-300. The fractions of these
303 primary emissions are higher in winter and autumn, possibly indicating higher emissions. Another
304 possibility is that the oxidation degradation of these primary emissions is faster in summer and spring
305 due to higher oxidants and ambient temperature. The contributions of photooxidation factors are 20-
306 70% to the total organic signals in the m/z range of 100-300, with the highest in summer, and lowest
307 in winter. This is consistent with the highest CHO organic fractions in UFPs in summer in Figure 1
308 and is attributed to the strongest solar radiation. The contributions of aqueous/heterogeneous sources
309 are 15-60% to the total organic signals in the m/z range of 100-300, with the highest in winter and
310 lowest in summer.

311 To identify the sources for UFP numbers, we further combined the source analysis with variation in
312 particle size distributions. Among the identified four classes of composition sources, some are related
313 to the increase of UFP number concentrations, while others are related to the increase of UFP diameters.

314   The increase in UFP numbers is usually accompanied by the enhanced contribution of cooking- or

315   vehicle-related components or new particle formation events. An example is shown in Figure 4, a

316   relatively clean day with little interference from background aerosols. There are three periods where

317   UFP bursts were observed. During period 1, i.e., 6:00-9:00, a mode with a peak diameter at ~20 nm

318   appeared with a rapid increase in the vehicle tracer, $C_3N_3O_3H_2^-$. Compared to that before period 1, the

319   contribution of the vehicle-related factor increased from 7% to 25%. During period 2, i.e., 12:00-15:00,

320   new particle formation happens with a burst of particles at a peak diameter of 5-10 nm. Compared to

321   that before period 2, the contribution of the photooxidation-related factor increased from 64% to 92%.

322   This is consistent with our previous studies that slowly-desorbed CHO organics were the most

323   abundant compounds during NPF periods (Li et al., 2022a). During period 3, i.e., 18:00-22:00, a mode

324   with peak diameter at ~30 nm bursts, with a rapid increase in the cooking tracer, $C_{18}H_{31}O_2^-$. $C_{18}H_{31}O_2^-$

325   also has two minor peaks in the morning and noon time, consistent with the cooking activities.

326   Compared to that before period 3, the contribution of the cooking-related factor increased from 18%

327   to 67%. Thus, we conclude that the increase in UFP numbers in the three periods is mainly attributed

328   to the increase in vehicle emissions, new particle formations, and cooking emissions, respectively.
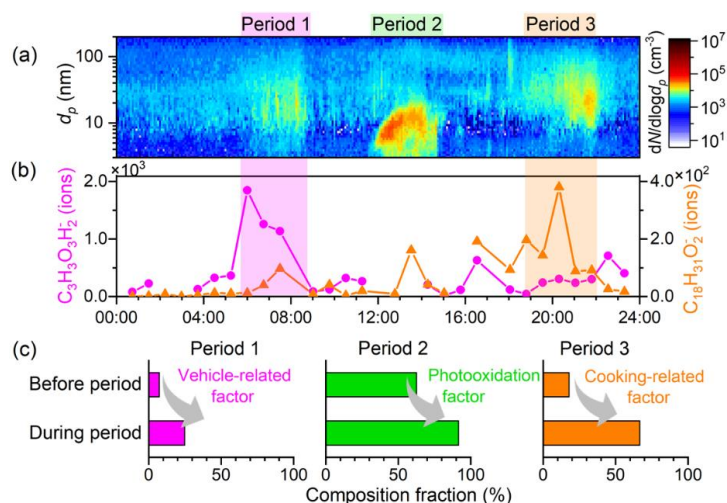
329

330   **Figure 4.** The particle number size distributions (a) and UFP composition variability (b-c) on April

331   16th, 2020. The three periods with the abrupt appearance of UFP particles on this day are identified as

332   vehicle-related (period 1), NPF-related (period 2), and cooking-related (period 3) according to

333   TDCIMS composition measurements.

334   The morning, noon, and evening peaks in UFP numbers were widely observed during the observation

335   days in all four seasons. During non-NPF days, the UFP number concentration peak mainly appears in

336   the morning and evening time, corresponding to the primary emissions, and we choose the morning

337   periods to calculate the daily-averaged E. During NPF days, the UFP number peak mainly appears in

338   the noon time, and the daily-averaged J was calculated during these periods. These further indicate

339   that cooking emissions, vehicle emissions, and new particle formation are the main sources of UFP

340   number concentrations.

341   Different from these three factors, the increased contribution of the aqueous/heterogeneous factor is

342   not accompanied by the increase of UFP number concentrations but by the increase of UFP mode

343   diameters. The contribution of aqueous/heterogeneous factor to sub-50 nm particles is only ~20%. For

344   example, in the day presented in Figure 4, aqueous/heterogeneous factor accounted less than ~10% for

345   the three bursts of UFP number concentration. However, it starts to dominate the organic composition

346   when UFP particles grow above 50 nm (Figure S12), indicating an important role of

347   aqueous/heterogeneous processes in the growth of particles larger than 50 nm in diameter.

348   **3.3 Driving factors for the seasonal variability of UFPs.**

349   As we have identified the main sources for UFP number concentrations in Section 3.2, we can further

350   address the reasons for the significant seasonal differences in UFP number concentrations as has been

351   shown in Figure 1, according to the variations in their sources and losses. The source terms mainly

352   include new particle formation rates (here represented by J_3) and primary emission rates (here

353   represented by E_{3-50}); the loss terms are presented by condensational growth rates (GR_{3-50}) and

354   coagulation sinks. Here, we apply the condensation sink (CS) to evaluate the strength of coagulation

355   loss.

356   The main sources of the UFP number concentration, J_3, and E_{3-50}, are both the highest in winter and

357   the lowest in summer (Figure 5a-b), which are presumably caused by temperature effects. The

358   temperature effect on J_3 is mainly due to the temperature-dependent cluster evaporation rates as

359   reported in our previous study (Deng et al., 2020). This seasonal dependence of atmospheric UFPs

360   attributed to vehicle emissions and its underlining reasons have not been revealed before. On the one

361   hand, the low ambient temperature will largely increase the vehicle emission factors for particle

362   numbers and gaseous hydrocarbons (Suarez-Bertoa and Astorga, 2018; Wen et al., 2021). On the other

363   hand, a large fraction of the nanoparticles from vehicle emissions has been proposed to be formed by

364   nucleation of the emitted hydrocarbon vapors or their oxidation products (Rönkkö and Timonen, 2019).

365   The high ambient temperatures in summer may suppress the formation of these vehicle-related

366   particles, just like it suppresses J_3 during ambient NPF.
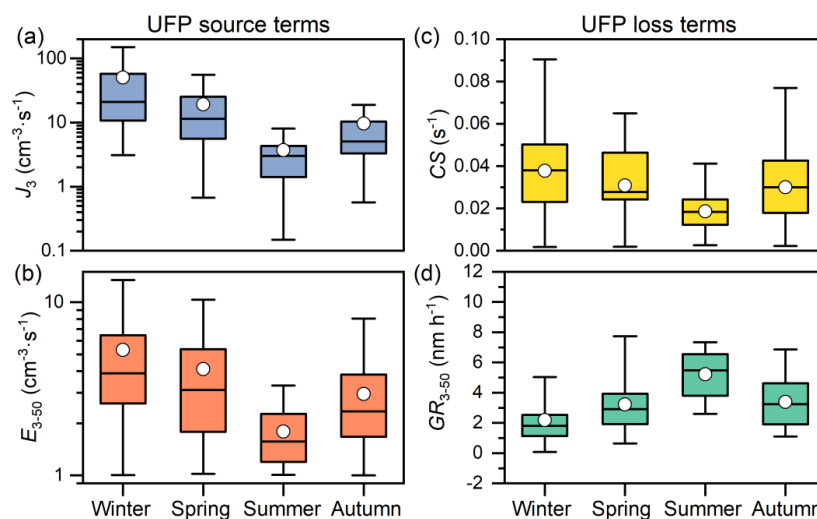
Figure 5. Seasonal variations of the main source and loss terms of UFP number concentration. (a) New particle formation rates for 3 nm particles (J_3); (b) daily average primary particle emission rates for 3-50 nm particles (E_{3-50}) during 6:00-9:00; (c) condensation sink (CS); (d) growth rates for 3-50 nm particles (GR_{3-50}) during new particle formation events using the mode fitting method.

The lowest GR of UFP occurs in winter (Figure 5d), which further contributes to high wintertime UFP number concentrations. CS and GR_{3-50} have opposite trends, with CS being the highest in winter while GR_{3-50} being the highest in summer (Figure 5c-d). The highest GR_{3-50} in summer is due to the highest condensable vapor concentrations in summer caused by strong solar radiation and high temperature favoring the formation of condensable OOMs (Li et al., 2022a; Qiao et al., 2021). The theoretical condensational GR by OOMs and H_2SO_4 for 20 nm particles are 1.1, 3.0, 4.0, and 1.8 nm·h^{-1} in winter, spring, summer, and autumn, respectively, and they are close to GR derived during NPF events using the mode-fitting method as shown in Figure 5d. Under the estimated GR, the time needed for sub-3 nm to grow above 50 and 100 nm is the shortest in summer (9 and 19 h, respectively), and the longest in winter (24 and 49 h, respectively). Thus, the lower GR in winter also contributes to the highest UFP number concentrations in winter.

4. Conclusions

In this study, we explored the UFP composition and sources in typical polluted urban environments based on near-continuous measurements of UFP composition and size distributions in Beijing over four seasons. We observed that UFP composition varied with seasons and particle diameter, indicating their different sources. Specifically, photooxidation processes generate more CHO organics, leading to higher CHO fractions in summer. While aqueous/heterogeneous processes generate more N- and S-containing organics, leading to higher N- and S-containing organic fractions in above-50 nm particles

390   than sub-50 nm particles. Combining the PMF analysis for UFP organics and the size distribution
391   analysis, we found that vehicle and cooking emissions are two of the most important primary sources
392   of UFP number concentrations in urban Beijing, while new particle formation is the most important
393   secondary source of UFP number concentrations and would increase the contribution of CHO organics
394   to UFP composition. The aqueous/heterogeneous sources would not increase UFP number
395   concentration but would increase UFP mode diameters and mass concentrations. For the seasonal
396   variations, we found that UFP number concentrations are the highest in winter. This is mainly due to
397   the highest primary particle emissions, the highest new particle formation rates, and the lowest particle
398   growth rates in winter. Further controlling of UFPs in urban Beijing needs to focus on vehicle
399   emissions, and the gas precursors related to secondary sources of UFPs.

400   The observed distinct seasonal variabilities of UFP composition and their size dependence emphasize
401   the importance of long-term and high-time-resolution measurements of both UFP composition and size
402   distributions. This could provide valuable datasets for the evaluation of UFP's long-term exposure risks.
403   The high time-resolution measurements combined with PMF analysis can also help identify the
404   secondary UFP sources, which contribute the major fraction of organic signals but could not be
405   identified from previous offline UFP measurements. Further addressing the UFP composition and
406   sources on the regional scale still requires measurements at sites with different distances from the
407   emission sources due to the short lifetime of UFPs.

408

409   **Data availability.**

410   Data are available upon request from the corresponding authors.

411   **Supplement.**

412   The contents of the supporting information include the diurnal variations of $E_{3\text{-}50}$ during non-NPF days
413   over four seasons (Figure S1); the diurnal variations of MLH, UVB, T, RH, O_3, NO_x, and $PM_{2.5}$ in the
414   four seasons (Figure S2); details of the measured UFP composition during four seasons (Figure S3);
415   seasonal variation of the UFP mass estimated from TDCIMS and PSD (Figure S4); the averaged
416   thermal desorption profiles of different UFP composition (Figure S5); the diurnal variation of CHO
417   organics in the four seasons (Figure S6); temperature dependence of some fast-desorbed UFP
418   composition (Figure S7); the spectra of five PMF-factors during spring, summer, and autumn (Figure
419   S8-10); summary of PMF factors during the four seasons (Figure S11); the contribution of different
420   factors as a function of particle sizes (Figure S12); summary of sampling periods (Table S1).

421   **Author contributions.**

422   XL, JJ, and JS designed the study. XL, YC, YYL, RC, YRL, and CD participated in data collection

423   and performed the data analysis. XL prepared the manuscript with contributions from all co-authors.

424   All authors approved the final version of the manuscript.

425   **Competing interests.**

426   The authors declare that they have no conflict of interest.

431

432   **References**

433   Cabada, J. C., Rees, S., Takahama, S., Khlystov, A., Pandis, S. N., Davidson, C. I., and Robinson, A.

434   L.: Mass size distributions and size resolved chemical composition of fine particulate matter at the

435   Pittsburgh supersite, Atmos. Environ., 38, 3127-3141, 10.1016/j.atmosenv.2004.03.004, 2004.

436   Cai, R., and Jiang, J.: A new balance formula to estimate new particle formation rate: reevaluating the

437   effect of coagulation scavenging, Atmos. Chem. Phys., 17, 12659-12675, 2017.

438   Cai, R., Yang, D., Fu, Y., Wang, X., Li, X., Ma, Y., Hao, J., Zheng, J., and Jiang, J.: Aerosol surface

439   area concentration: a governing factor in new particle formation in Beijing, Atmos. Chem. Phys., 17,

440   12327, 2017.

441   Cai, R., Chandra, I., Yang, D., Yao, L., Fu, Y., Li, X., Lu, Y., Luo, L., Hao, J., Ma, Y., Wang, L., Zheng,

442   J., Seto, T., and Jiang, J.: Estimating the influence of transport on aerosol size distributions during new

443   particle formation events, Atmos. Chem. Phys., 18, 16587-16599, 10.5194/acp-18-16587-2018, 2018.

444   Canonaco, F., Crippa, M., Slowik, J., Baltensperger, U., and Prévôt, A.: SoFi, an IGOR-based interface

445   for the efficient use of the generalized multilinear engine (ME-2) for the source apportionment: ME-2

446   application to aerosol mass spectrometer data, Atmos. Meas. Tech., 6, 3649, 2013.

447   Cass, G. R., Hughes, L. A., Bhave, P., Kleeman, M. J., Allen, J. O., and Salmon, L. G.: The chemical

448   composition of atmospheric ultrafine particles, Philosophical Transactions of the Royal Society of

449   London   Series   a-Mathematical   Physical   and   Engineering   Sciences,   358,   2581-2592,

450   10.1098/rsta.2000.0670, 2000.

451   Deng, C., Fu, Y., Dada, L., Yan, C., Cai, R., Yang, D., Zhou, Y., Yin, R., Lu, Y., Li, X., Qiao, X., Fan,

452   X., Nie, W., Kontkanen, J., Kangasluoma, J., Chu, B., Ding, A., Kerminen, V.-M., Paasonen, P.,

453   Worsnop, D. R., Bianchi, F., Liu, Y., Zheng, J., Wang, L., Kulmala, M., and Jiang, J.: Seasonal

454   Characteristics of New Particle Formation and Growth in Urban Beijing, Environ. Sci. Technol., 54,

455   8547–8557, 10.1021/acs.est.0c00808, 2020.

456   Eresmaa, N., Harkonen, J., Joffre, S. M., Schultz, D. M., Karppinen, A., and Kukkonen, J.: A Three-

457   Step Method for Estimating the Mixing Height Using Ceilometer Data from the Helsinki Testbed,

458   Journal of Applied Meteorology and Climatology, 51, 2172-2187, 10.1175/jamc-d-12-058.1, 2012.

459 Glicker, H. S., Lawler, M. J., Ortega, J., de Sá, S. S., Martin, S. T., Artaxo, P., Vega Bustillos, O., de
460 Souza, R., Tota, J., Carlton, A., and Smith, J. N.: Chemical composition of ultrafine aerosol particles
461 in central Amazonia during the wet season, Atmos. Chem. Phys., 19, 13053-13066, 10.5194/acp-19-
462 13053-2019, 2019.
463 Ham, W. A., and Kleeman, M. J.: Size-resolved source apportionment of carbonaceous particulate
464 matter in urban and rural sites in central California, Atmos. Environ., 45, 3988-3995,
465 10.1016/j.atmosenv.2011.04.063, 2011.
466 Understanding   the   Health   Effects   of   Ambient   Ultrafine   Particles:
467 https://www.healtheffects.org/publication/understanding-health-effects-ambient-ultrafine-particles,
468 access: Jan 26th, 2019, 2013.
469 Herner, J. D., Aw, J., Gao, O., Chang, D. P., and Kleeman, M. J.: Size and composition distribution of
470 airborne particulate matter in northern California: I-particulate mass, carbon, and water-soluble ions,
471 J. Air Waste Manage., 55, 30-51, 10.1080/10473289.2005.10464600, 2005.
472 Hu, W., Hu, M., Hu, W.-W., Zheng, J., Chen, C., Wu, Y., and Guo, S.: Seasonal variations in high time-
473 resolved chemical compositions, sources, and evolution of atmospheric submicron aerosols in the
474 megacity Beijing, Atmos. Chem. Phys., 17, 9979-10000, 10.5194/acp-17-9979-2017, 2017.
475 Kleeman, M. J., Riddle, S. G., Robert, M. A., Jakober, C. A., Fine, P. M., Hays, M. D., Schauer, J. J.,
476 and Hannigan, M. P.: Source Apportionment of Fine (PM1.8) and Ultrafine (PM0.1) Airborne
477 Particulate Matter during a Severe Winter Pollution Episode, Environ. Sci. Technol., 43, 272-279,
478 10.1021/es800400m, 2009.
479 Kontkanen, J., Deng, C., Fu, Y., Dada, L., Zhou, Y., Cai, J., Daellenbach, K. R., Hakala, S., Kokkonen,
480 T. V., Lin, Z., Liu, Y., Wang, Y., Yan, C., Petäjä, T., Jiang, J., Kulmala, M., and Paasonen, P.: Size-
481 resolved particle number emissions in Beijing determined from measured particle size distributions,
482 Atmos. Chem. Phys., 20, 11329-11348, 10.5194/acp-20-11329-2020, 2020.
483 Kulmala, M., Vehkamäki, H., Petäjä, T., Dal Maso, M., Lauri, A., Kerminen, V. M., Birmili, W., and
484 McMurry, P. H.: Formation and growth rates of ultrafine atmospheric particles: a review of
485 observations, J. Aerosol. Sci., 35, 143–176, 10.1016/j.jaerosci.2003.10.003, 2004.
486 Lawler, M. J., Whitehead, J., O'Dowd, C., Monahan, C., McFiggans, G., and Smith, J. N.: Composition
487 of 15-85 nm particles in marine air, Atmos. Chem. Phys., 14, 11557–11569, 10.5194/acp-14-11557-
488 2014, 2014.
489 Lawler, M. J., Rissanen, M. P., Ehn, M., Mauldin, R. L., Sarnela, N., Sipilä, M., and Smith, J. N.:
490 Evidence for Diverse Biogeochemical Drivers of Boreal Forest New Particle Formation, Geophys. Res.
491 Lett., 45, 2038–2046, doi:10.1002/2017GL076394, 2018.
492 Lawler, M. J., Draper, D. C., and Smith, J. N.: Atmospheric fungal nanoparticle bursts, Sci. Adv., 6,
493 No. eaax9051, 10.1126/sciadv.aax9051, 2020.
494 Lawler, M. J., Saltzman, E. S., Karlsson, L., Zieger, P., Salter, M., Baccarini, A., Schmale, J., and Leck,
495 C.: New Insights Into the Composition and Origins of Ultrafine Aerosol in the Summertime High
496 Arctic, Geophys. Res. Lett., 48, 10.1029/2021gl094395, 2021.
497 Li, H., Zhong, J., Vehkamaki, H., Kurten, T., Wang, W., Ge, M., Zhang, S., Li, Z., Zhang, X., Francisco,
498 J. S., and Zeng, X. C.: Self-Catalytic Reaction of SO3 and NH3 To Produce Sulfamic Acid and Its
499 Implication to Atmospheric Particle Formation, J. Am. Chem. Soc., 140, 11020-11028,

500   10.1021/jacs.8b04928, 2018.

501   Li, X., Zhao, B., Zhou, W., Shi, H., Yin, R., Cai, R., Yang, D., Dallenbach, K., Deng, C., Fu, Y., Qiao,
502   X., Wang, L., Liu, Y., Yan, C., Kulmala, M., Zheng, J., Hao, J., Wang, S., and Jiang, J.: Responses of
503   gaseous sulfuric acid and particulate sulfate to reduced SO2 concentration: A perspective from long-
504   term measurements in Beijing, Sci. Total Environ., 721, No. 137700, 10.1016/j.scitotenv.2020.137700,
505   2020.

506   Li, X., Li, Y., Lawler, M. J., Hao, J., Smith, J. N., and Jiang, J.: Composition of Ultrafine Particles in
507   Urban Beijing: Measurement Using a Thermal Desorption Chemical Ionization Mass Spectrometer,
508   Environ. Sci. Technol., 55, 2859–2868, 10.1021/acs.est.0c06053, 2021.

509   Li, X., Li, Y., Cai, R., Yan, C., Qiao, X., Guo, Y., Deng, C., Yin, R., Chen, Y., Li, Y., Yao, L., Sarnela,
510   N., Zhang, Y., Petäjä, T., Bianchi, F., Liu, Y., Kulmala, M., Hao, J., Smith, J. N., and Jiang, J.:
511   Insufficient Condensable Organic Vapors Lead to Slow Growth of New Particles in an Urban
512   Environment, Environ. Sci. Technol., 55, 9936-9946, 10.1021/acs.est.2c01566, 2022a.

513   Li, X., Sun, N., Jin, Q., Zhao, Z., Wang, L., Wang, Q., Gu, X., Li, Y., and Liu, X.: Light absorption
514   properties of black and brown carbon in winter over the North China Plain: Impacts of regional
515   biomass burning, Atmos. Environ., 278, 10.1016/j.atmosenv.2022.119100, 2022b.

516   Liu, Y., Yan, C., Feng, Z., Zheng, F., Fan, X., Zhang, Y., Li, C., Zhou, Y., Lin, Z., Guo, Y., Zhang, Y.,
517   Ma, L., Zhou, W., Liu, Z., Dada, L., Daellenbach, K., Kontkanen, J., Cai, R., Chan, T., and Kulmala,
518   M.: Continuous and comprehensive atmospheric observations in Beijing: a station to understand the
519   complex   urban   atmospheric   environment,   Big   Earth   Data,   4,   295-321,
520   10.1080/20964471.2020.1798707, 2020.

521   Ma, J., Ungeheuer, F., Zheng, F., Du, W., Wang, Y., Cai, J., Zhou, Y., Yan, C., Liu, Y., Kulmala, M.,
522   Daellenbach, K. R., and Vogel, A. L.: Nontarget Screening Exhibits a Seasonal Cycle of PM2.5
523   Organic Aerosol Composition in Beijing, Environ. Sci. Technol., 10.1021/acs.est.1c06905, 2022.

524   Massling, A., Stock, M., Wehner, B., Wu, Z. J., Hu, M., Brueggemann, E., Gnauk, T., Herrmann, H.,
525   and Wiedensohler, A.: Size segregated water uptake of the urban submicrometer aerosol in Beijing,
526   Atmos. Environ., 43, 1578-1589, 10.1016/j.atmosenv.2008.06.003, 2009.

527   Municipality, t. P. s. G. o. B.: The implementation of forbidden area for high-polluting fuels in Beijing,
528   http://www.beijing.gov.cn/zhengce/zfwj/zfwj/szfwj/201905/t20190523_72669.html, 2014.

529   Oberdorster, G., Oberdorster, E., and Oberdorster, J.: Nanotoxicology: an emerging discipline evolving
530   from studies of ultrafine particles, Environ Health Perspect, 113, 823-839, 10.1289/ehp.7339, 2005.

531   Ohlwein, S., Kappeler, R., Kutlar Joss, M., Kunzli, N., and Hoffmann, B.: Health effects of ultrafine
532   particles: a systematic literature review update of epidemiological evidence, Int J Public Health, 64,
533   547-559, 10.1007/s00038-019-01202-7, 2019.

534   Organization, W. H.: WHO global air quality guidelines: particulate matter (PM2.5 and PM10), ozone,
535   nitrogen   dioxide,   sulfur   dioxide   and   carbon   monoxide,
536   https://apps.who.int/iris/bitstream/handle/10665/345329/9789240034228-eng.pdf, 2021.

537   Pierce, J. R., and Adams, P. J.: Efficiency of cloud condensation nuclei formation from ultrafine
538   particles, Atmos. Chem. Phys., 7, 1367-1379, 2007.

539   Qiao, X., Yan, C., Li, X., Guo, Y., Yin, R., Deng, C., Li, C., Nie, W., Wang, M., Cai, R., Huang, D.,
540   Wang, Z., Yao, L., Worsnop, D. R., Bianchi, F., Liu, Y., Donahue, N. M., Kulmala, M., and Jiang, J.:

541 Contribution of Atmospheric Oxygenated Organic Compounds to Particle Growth in an Urban
542 Environment, Environ. Sci. Technol., 55, 13646–13656, 10.1021/acs.est.1c02095, 2021.
543 Rönkkö, T., and Timonen, H.: Overview of Sources and Characteristics of Nanoparticles in Urban
544 Traffic-Influenced Areas, Journal of Alzheimer's Disease, 72, 1-14, 10.3233/JAD-190170, 2019.
545 Sarkar, S., Oram, B. K., and Bandyopadhyay, B.: Influence of Ammonia and Water on the Fate of
546 Sulfur Trioxide in the Troposphere: Theoretical Investigation of Sulfamic Acid and Sulfuric Acid
547 Formation Pathways, J. Phys. Chem. A., 123, 3131-3141, 10.1021/acs.jpca.8b09306, 2019.
548 Smith, J. N., Moore, K. F., McMurry, P. H., and Eisele, F. L.: Atmospheric measurements of sub-20
549 nm diameter particle chemical composition by thermal desorption chemical ionization mass
550 spectrometry, Aerosol Sci. Tech., 38, 100–110, 10.1080/02786820490249036, 2004.
551 Smith, J. N., Moore, K. F., Eisele, F. L., Voisin, D., Ghimire, A. K., Sakurai, H., and McMurry, P. H.:
552 Chemical composition of atmospheric nanoparticles during nucleation events in Atlanta, J. Geophys.
553 Res-Atmos., 110, No. D22S03, 10.1029/2005jd005912, 2005.
554 Smith, J. N., Dunn, M. J., VanReken, T. M., Iida, K., Stolzenburg, M. R., McMurry, P. H., and Huey,
555 L. G.: Chemical composition of atmospheric nanoparticles formed from nucleation in Tecamac,
556 Mexico: Evidence for an important role for organic species in nanoparticle growth, Geophys. Res.
557 Lett., 35, No. L4808, 10.1029/2007gl032523, 2008.
558 Smith, J. N., Barsanti, K. C., Friedli, H. R., Ehn, M., Kulmala, M., Collins, D. R., Scheckman, J. H.,
559 Williams, B. J., and McMurry, P. H.: Observations of aminium salts in atmospheric nanoparticles and
560 possible climatic implications, Proc. Natl. Acad. Sci. U.S.A., 107, 6634–6639,
561 10.1073/pnas.0912127107, 2010.
562 Suarez-Bertoa, R., and Astorga, C.: Impact of cold temperature on Euro 6 passenger car emissions,
563 Environ. Pollut., 234, 318-329, 10.1016/j.envpol.2017.10.096, 2018.
564 Sun, Y., Xu, W., Zhang, Q., Jiang, Q., Canonaco, F., Prévôt, A. S. H., Fu, P., Li, J., Jayne, J., Worsnop,
565 D. R., and Wang, Z.: Source apportionment of organic aerosol from 2-year highly time-resolved
566 measurements by an aerosol chemical speciation monitor in Beijing, China, Atmos. Chem. Phys., 18,
567 8469-8489, 10.5194/acp-18-8469-2018, 2018.
568 Sun, Y. L., Wang, Z. F., Du, W., Zhang, Q., Wang, Q. Q., Fu, P. Q., Pan, X. L., Li, J., Jayne, J., and
569 Worsnop, D. R.: Long-term real-time measurements of aerosol particle composition in Beijing, China:
570 seasonal variations, meteorological effects, and source analysis, Atmos. Chem. Phys., 15, 10149-10165,
571 10.5194/acp-15-10149-2015, 2015.
572 Wen, Y., Zhang, S., He, L., Yang, S., Wu, X., and Wu, Y.: Characterizing start emissions of gasoline
573 vehicles and the seasonal, diurnal and spatial variabilities in China, Atmos. Environ., 245,
574 10.1016/j.atmosenv.2020.118040, 2021.
575 WHO: Review of evidence on health aspects of air pollution — REVIHAAP. World Health
576 Organisation, World Health Organisation, Regional Office for Europe,
577 https://www.euro.who.int/__data/assets/pdf_file/0020/182432/e96762-final.pdf, 2013.
578 Winkler, P. M., Ortega, J., Karl, T., Cappellin, L., Friedli, H. R., Barsanti, K., McMurry, P. H., and
579 Smith, J. N.: Identification of the biogenic compounds responsible for size-dependent nanoparticle
580 growth, Geophys. Res. Lett., 39, No. L20815, 10.1029/2012gl053253, 2012.
581 Wu, Z., Hu, M., Liu, S., Wehner, B., Bauer, S., Ma ßling, A., Wiedensohler, A., Petäjä, T., Dal Maso,

582 M., and Kulmala, M.: New particle formation in Beijing, China: Statistical analysis of a 1-year data
583 set, J. Geophys. Res., 112, 10.1029/2006jd007406, 2007.
584 Xu, S., Ren, L., Lang, Y., Hou, S., Ren, H., Wei, L., Wu, L., Deng, J., Hu, W., Pan, X., Sun, Y., Wang,
585 Z., Su, H., Cheng, Y., and Fu, P.: Molecular markers of biomass burning and primary biological
586 aerosols in urban Beijing: size distribution and seasonal variation, Atmos. Chem. Phys., 20, 3623-3644,
587 10.5194/acp-20-3623-2020, 2020.
588 Xue, J., Xue, W., Sowlat, M. H., Sioutas, C., Lolinco, A., Hasson, A., and Kleeman, M. J.: Seasonal
589 and Annual Source Appointment of Carbonaceous Ultrafine Particulate Matter (PM0.1) in Polluted
590 California Cities, Environ. Sci. Technol., 53, 39-49, 10.1021/acs.est.8b04404, 2019.
591 Xue, W., Xue, J., Mousavi, A., Sioutas, C., and Kleeman, M. J.: Positive matrix factorization of
592 ultrafine particle mass (PM0.1) at three sites in California, Sci. Total Environ., 715,
593 10.1016/j.scitotenv.2020.136902, 2020a.
594 Xue, W., Xue, J., Shirmohammadi, F., Sioutas, C., Lolinco, A., Hasson, A., and Kleeman, M. J.: Day-
595 of-week patterns for ultrafine particulate matter components at four sites in California, Atmos.
596 Environ., 222, 10.1016/j.atmosenv.2019.117088, 2020b.
597 Yan, C., Nie, W., Vogel, A. L., Dada, L., Lehtipalo, K., Stolzenburg, D., Wagner, R., Rissanen, M. P.,
598 Xiao, M., Ahonen, L., Fischer, L., Rose, C., Bianchi, F., Gordon, H., Simon, M., Heinritzi, M.,
599 Garmash, O., Roldin, P., Dias, A., Ye, P., Hofbauer, V., Amorim, A., Bauer, P. S., Bergen, A.,
600 Bernhammer, A. K., Breitenlechner, M., Brilke, S., Buchholz, A., Mazon, S. B., Canagaratna, M. R.,
601 Chen, X., Ding, A., Dommen, J., Draper, D. C., Duplissy, J., Frege, C., Heyn, C., Guida, R., Hakala,
602 J., Heikkinen, L., Hoyle, C. R., Jokinen, T., Kangasluoma, J., Kirkby, J., Kontkanen, J., Kuerten, A.,
603 Lawler, M. J., Mai, H., Mathot, S., Mauldin, R. L., III, Molteni, U., Nichman, L., Nieminen, T., Nowak,
604 J., Ojdanic, A., Onnela, A., Pajunoja, A., Petaja, T., Piel, F., Quelever, L. L. J., Sarnela, N., Schallhart,
605 S., Sengupta, K., Sipila, M., Tome, A., Troestl, J., Vaisanen, O., Wagner, A. C., Ylisirnio, A., Zha, Q.,
606 Baltensperger, U., Carslaw, K. S., Curtius, J., Flagan, R. C., Hansel, A., Riipinen, I., Smith, J. N.,
607 Virtanen, A., Winkler, P. M., Donahue, N. M., Kerminen, V. M., Kulmala, M., Ehn, M., and Worsnop,
608 D. R.: Size-dependent influence of NOx on the growth rates of organic aerosol particles, Sci. Adv., 6,
609 eaay4945, 10.1126/sciadv.aay4945, 2020.
610 Yassine, M. M., Dabek-Zlotorzynska, E., and Celo, V.: Development of a hydrophilic interaction liquid
611 chromatography-mass spectrometry method for detection and quantification of urea thermal
612 decomposition by-products in emission from diesel engine employing selective catalytic reduction
613 technology, Journal of Chromatography A, 1229, 208-215, 10.1016/j.chroma.2012.01.046, 2012.
614 Ye, Q., Wang, M., Hofbauer, V., Stolzenburg, D., Chen, D., Schervish, M., Vogel, A., Mauldin, R. L.,
615 Baalbaki, R., Brilke, S., Dada, L., Dias, A., Duplissy, J., El Haddad, I., Finkenzeller, H., Fischer, L.,
616 He, X., Kim, C., Kuerten, A., Lamkaddam, H., Lee, C. P., Lehtipalo, K., Leiminger, M., Manninen, H.
617 E., Marten, R., Mentler, B., Partoll, E., Petaja, T., Rissanen, M., Schobesberger, S., Schuchmann, S.,
618 Simon, M., Tham, Y. J., Vazquez-Pufleau, M., Wagner, A. C., Wang, Y., Wu, Y., Xiao, M.,
619 Baltensperger, U., Curtius, J., Flagan, R., Kirkby, J., Kulmala, M., Volkamer, R., Winkler, P. M.,
620 Worsnop, D., and Donahue, N. M.: Molecular Composition and Volatility of Nucleated Particles from
621 alpha-Pinene Oxidation between-50 degrees C and+25 degrees C, Environ. Sci. Technol., 53, 12357–
622 12365, 10.1021/acs.est.9b03265, 2019.

623   Zhang, R., Jing, J., Tao, J., Hsu, S. C., Wang, G., Cao, J., Lee, C. S. L., Zhu, L., Chen, Z., Zhao, Y.,
624   and Shen, Z.: Chemical characterization and source apportionment of PM2.5 in Beijing: seasonal
625   perspective, Atmos. Chem. Phys., 13, 7053-7074, 10.5194/acp-13-7053-2013, 2013.
626   Zhang, T., Claeys, M., Cachier, H., Dong, S., Wang, W., Maenhaut, W., and Liu, X.: Identification and
627   estimation of the biomass burning contribution to Beijing aerosol using levoglucosan as a molecular
628   marker, Atmos. Environ., 42, 7013-7021, 10.1016/j.atmosenv.2008.04.050, 2008.
629   Zhao, P., Chen, Y., and Su, J.: Size-resolved carbonaceous components and water-soluble ions
630   measurements of ambient aerosol in Beijing, J. Environ. Sci., 54, 298-313, 10.1016/j.jes.2016.08.027,
631   2017.
632   Zhao, Y., Hu, M., Slanina, S., and Zhang, Y.: The molecular distribution of fine particulate organic
633   matter emitted from Western-style fast food cooking, Atmos Environ, 41, 8163-8171,
634   10.1016/j.atmosenv.2007.06.029, 2007a.
635   Zhao, Y., Hu, M., Slanina, S., and Zhang, Y.: Chemical compositions of fine particulate organic matter
636   emitted from Chinese cooking, Environ Sci Technol, 41, 99-105, 10.1021/es0614518, 2007b.

637